A Cohesive Element Model for Large-Scale Crash Analyses in LS-DYNA®

Johan Kolstø Sønstabø[a], David Morin[a], Magnus Langseth[a]

Structural Impact Laboratory (SIMLab) and Centre for Advanced Structural Analysis (CASA), Department of Structural Engineering, Norwegian University of Science and Technology, Rich. Birkelandsvei 1a, N-7491 Trondheim, Norway

Abstract

*In a recent study the cohesive element model *MAT_240 was evaluated for macroscopic modelling of two different Flow-Drill Screw (FDS) connections in large-scale analyses [1]. The study showed that *MAT_240 does not have sufficient flexibility to describe the macroscopic behaviour of the connections. In particular, the force level and initial stiffness in mixed-mode loadings were severely over-estimated. The lack of flexibility to control the mixed-mode behaviour was also pointed out by Sommer and Maier [2], who investigated self-piercing rivet connections.*

*This paper presents a new cohesive element model for use in LS-DYNA. The model is based on *MAT_240, presented by Marzi, et al. [3], with added flexibility to control the behaviour under mixed-mode loadings.*

Introduction

In the continuous effort to reduce weight, connection techniques such as self-piercing riveting (SPR) and flow-drill screw driving (FDS) has become common to join dissimilar aluminium alloys in the load-bearing structure of vehicles. Due to time-step limitations, such connections cannot be included in large-scale FE simulations in their physical form. To include them and their important effect on the structural response, simplified macroscopic modelling techniques are used.

One technique that has been employed involves using a single or a cluster of cohesive elements tied between two shell surfaces. By calibrating the assigned cohesive element model (which typically is developed to model structural bonding) to mechanical tests of the connections, the macroscopic behaviour of the connections may to some extent be captured.

This approach was investigated by Sommer and Maier [2] who applied the models *MAT_240 [3] and *MAT_169 [4] to model an SPR connection. According to their findings *MAT_240 was most promising, but they pointed out that there was no parameter to control the mixed-mode behaviour and that this was a weakness of the model. Bier, et al. [5] investigated the ability of *MAT_240 to model spot welds, and found that the model was beneficial in some load cases, especially in shear. In a recent study by the present authors, the lack of flexibility to control the mixed mode was demonstrated for two different FDS connections [1].

This paper presents a new cohesive element model for use in LS-DYNA. The model is heavily based on *MAT_240, presented by Marzi, et al. [3], with added flexibility to control the behaviour under mixed-mode loadings. The model is demonstrated for one SPR and two different FDS connections, and it is shown that the ability to model FDS connections is enhanced.

Model Description

As *MAT_240, the new model incorporates linear elasticity, ideal plasticity and linear softening, and calculates the stresses in the integration points based on the relative displacement between the upper and lower surfaces of the element. This section presents the model theory in detail.

The displacements in normal and tangential directions, Δ_n and Δ_t, are calculated as

$$\Delta_n = \langle u_n \rangle \tag{1}$$

$$\Delta_t = \sqrt{u_{t1} + u_{t2}}, \tag{2}$$

where u_n, u_{t1} and u_{t2} are the normal and the two tangential element displacements in the element coordinate system, respectively. The brackets in equation (1) denote the Macaulay brackets. The total displacement is then determined as

$$\Delta_m = \sqrt{\Delta_n^2 + \Delta_t^2}. \tag{3}$$

Figure 1 shows the tri-linear stress-displacement curve for pure normal (tensile) and pure tangential (shear) loading. The shape of the curves are determined with user-parameters as follows. In pure tension, N is the yield stress, δ_{n1} is the yield displacement, δ_{n2} is the damage initiation displacement, and δ_{n3} is the failure displacement. The corresponding parameters for pure shear are T, δ_{t1}, δ_{t2} and δ_{t3}, respectively. These parameters must be determined from experiments. The stiffness in normal and shear direction is computed as $E_n = \frac{N}{\delta_{n1}}$ and $E_t = \frac{T}{\delta_{t1}}$, respectively.

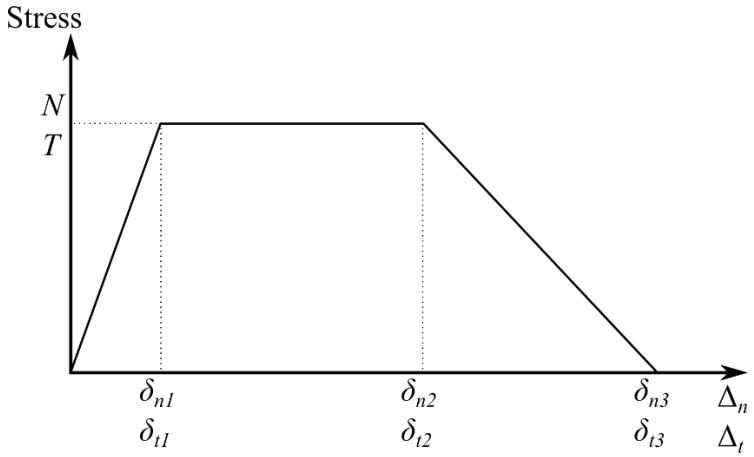

Figure 1: Stress-displacement curve for pure normal and pure tangential loading. After [3].

The shape of the mixed-mode (total) stress-displacement curve is a function of the mode mixity. The ratio of normal and tangential displacements defines the mode mixity angle γ as follows,

$$\gamma = \arctan\frac{\Delta_n}{\Delta_t}. \tag{4}$$

Thus, $\gamma = 0$ for pure normal loading and $\gamma = \frac{\pi}{2}$ for pure tangential loading. The yield-, damage initiation- and failure displacements in mixed mode are calculated as

$$\delta_{m1} = \frac{\delta_{n1}\delta_{t1}}{[(\delta_{t1}\cos\gamma_1)^{\alpha_1} + (\delta_{n1}\sin\gamma_1)^{\alpha_1}]^{1/\alpha_1}} \tag{5}$$

$$\delta_{m2} = \frac{\delta_{n2}\delta_{t2}}{[(\delta_{t2}\cos\gamma_2)^{\alpha_2} + (\delta_{n2}\sin\gamma_2)^{\alpha_2}]^{1/\alpha_2}} \tag{6}$$

$$\delta_{m3} = \frac{\delta_{n3}\delta_{t3}}{[(\delta_{t3}\cos\gamma_3)^{\alpha_3} + (\delta_{n3}\sin\gamma_3)^{\alpha_3}]^{1/\alpha_3}}, \tag{7}$$

respectively, where

$$\gamma_1 = \arctan\left(\frac{\Delta_n}{\Delta_t}\frac{\delta_{t1}}{\delta_{n1}}\right) \tag{8}$$

$$\gamma_2 = \arctan\left(\frac{\Delta_n}{\Delta_t}\frac{\delta_{t2}}{\delta_{n2}}\right) \tag{9}$$

$$\gamma_3 = \arctan\left(\frac{\Delta_n}{\Delta_t}\frac{\delta_{t3}}{\delta_{n3}}\right). \tag{10}$$

The angles $\gamma_i, i = 1,2,3$ are mode mixity angles normalized such that they are equal to $\pi/4$ when $\frac{\Delta_n}{\delta_{ni}} = \frac{\Delta_t}{\delta_{ti}}$, as illustrated in Figure 2. Equation (5), (6) and (7) describe super-ellipses in the normalized displacement plane (see Figure 3), whose shape is governed by the user-parameters α_1, α_2 and α_3. The parameters define the shape of the mixed-mode stress-displacement curve as function of mode mixity (see Figure 4). For $\alpha_1 = \alpha_2 = 2$ the quadratic formulas of *MAT_240 [3] are retained.

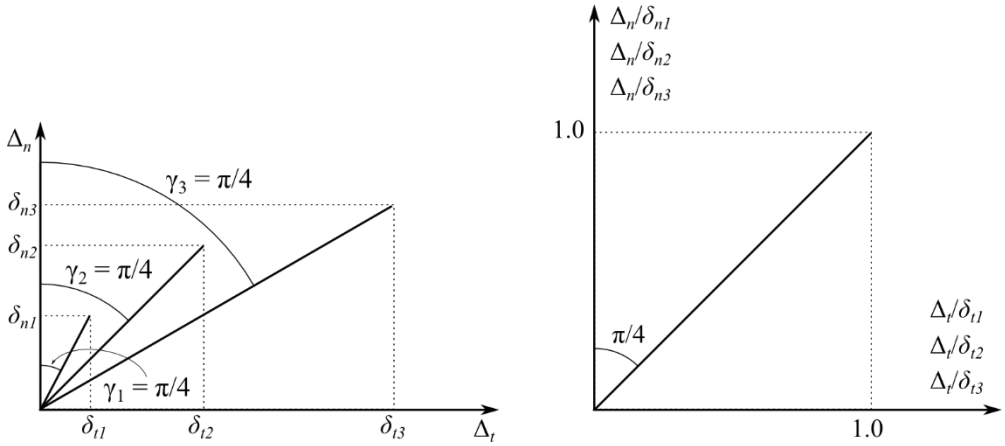

Figure 2: Illustration of normalized mode mixity angles in displacement plane (left) and normalized displacement plane (right).

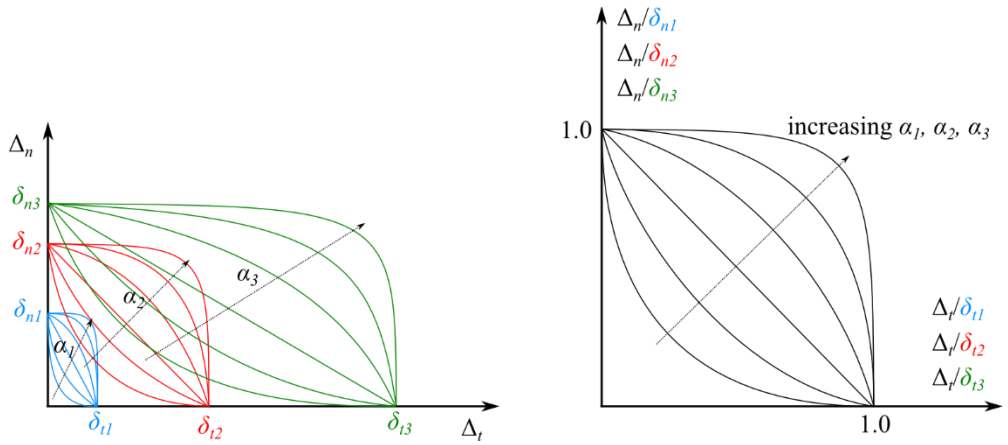

Figure 3: Interaction curves for yield-, damage initiation- and failure displacements in displacement plane (left) and normalized displacement plane (right).

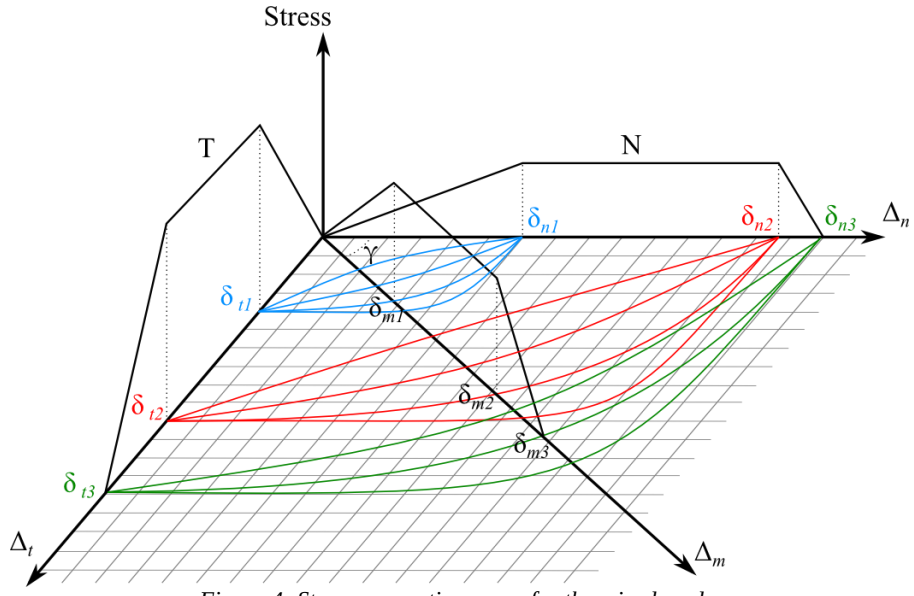

Figure 4: Stress-separation curve for the mixed mode.

Now the plastic part of the displacements in each element direction, u_n^p, u_{t1}^p and u_{t2}^p, may be calculated. In the normal direction it is given by

$$u_n^p = \max\left(u_{n,\Delta t-1}^p, u_n - \delta_{m1}\cos\gamma\,, 0\right), \tag{11}$$

where subscript $\Delta t - 1$ denotes the variable at the previous time step. Thus, if plasticity occurs, the plastic normal displacement is equal to the total normal displacement minus its elastic part. If the loading is purely elastic the plastic normal displacement remains zero or equal to the value at the previous time step.

For the shear direction, a shear yield displacement is defined as

$$\delta_{ty} = \sqrt{\left(u_{t1} - u_{t1,\Delta t-1}^p\right)^2 + \left(u_{t2} - u_{t2,\Delta t-1}^p\right)^2}. \tag{12}$$

If $\delta_{ty} > \delta_{m1}\sin\gamma$, plasticity occurs, and the displacement increments are added to the plastic displacements,

$$u_{t1}^p = u_{t1,\Delta t-1}^p + \left(u_{t1} - u_{t1,\Delta t-1}\right) \tag{13}$$

$$u_{t2}^{p} = u_{t2,\Delta t-1}^{p} + \left(u_{t2} - u_{t2,\Delta t-1}\right). \quad (14)$$

Softening is obtained with damage coupling. If $\Delta_m > \delta_{m2}$, a damage variable d increases linearly,

$$d = \max\left(\frac{\Delta_m - \delta_{m2}}{\delta_{m3} - \delta_{m2}}, d_{\Delta t-1}, 0\right). \quad (15)$$

When d reaches unity the integration point fails.

The stresses in the integration point may now be calculated from the elastic displacements. In normal direction softening is only considered under tensile loading. That is, if $u_n - u_n^p < 0$,

$$\sigma_n = E_n\left(u_n - u_n^p\right), \quad (16)$$

otherwise,

$$\sigma_n = E_n(1-d)\left(u_n - u_n^p\right). \quad (17)$$

The shear stresses are

$$\sigma_{t1} = E_t(1-d)\left(u_{t1} - u_{t1}^p\right) \quad (18)$$

$$\sigma_{t2} = E_t(1-d)\left(u_{t2} - u_{t2}^p\right). \quad (19)$$

Note that the model in the present form does not account for rate-dependency. This can be included analogous to *MAT_240, but this was not considered in this work.

Model validation

Experiments

To demonstrate the increased flexibility compared to *MAT_240, the new model and *MAT_240 were calibrated to three different sets of experimental data. The first two sets consisted of tests of a self-piercing rivet and a flow-drill screw connection between two aluminium sheets (alloy 6016 T4). These connections are henceforth denoted as *the SPR connection* and *the small FDS connection*, respectively. The third set consisted of tests of a flow-drill screw connection between an aluminium sheet (allow 6016 T4) and an aluminium extrusion (alloy 6063 T6). This connection is henceforth denoted as *the large FDS connection*. The screws in the two FDS connections were of different size and geometry. The nominal thicknesses of the sheet and extrusion was 2 mm. The tests on the SPR connection and the small screw connection has previously been published [1], and the tests on the large FDS connection has been submitted for publication. Each set of experiments consisted of cross tests in tension, shear and a mixed mode, and single lap-joint and peeling tests. All tests were quasi-static.

Figure 5 shows the cross test specimen and testing rig. As shown in the figure the specimens were inserted into the testing rig, which was clamped to the cross-head of the test machine. The cross-head force and displacement were measured during the tests. The testing rig was designed such that the load application line passed through the centre of the specimen. The global loading angle could be varied, giving different loadings on the connections. In this work, three different loading angles were considered: 90°, 45° and 0°, which corresponds to tension, combined tension and shear, and shear. The mechanical clamping of the plates in these tests constrained the deformation of the specimens such that the macroscopic deformation of the connections was approximately equal to the global displacement of the specimens. Thus, the macroscopic

displacement path was simple and to some extent known. These tests were therefore well suited for calibration.

Figure 6 and Figure 7 show illustrations of the single lap joint and peeling specimens, respectively. As shown, the geometry of the specimens with two sheets were slightly different from the specimens with an extrusion. The tests were performed by clamping each end (grey area in Figure 6 and Figure 7) and pulling in the longitudinal direction. In these tests, the macroscopic deformation of the connections was non-proportional and less controlled than in the cross tests. Using these two tests for validation therefore provided useful information regarding the ability of the cohesive element models to represent loadings that are more challenging.

Cf. [6] for a detailed description of the test set-up of all the single connector tests.

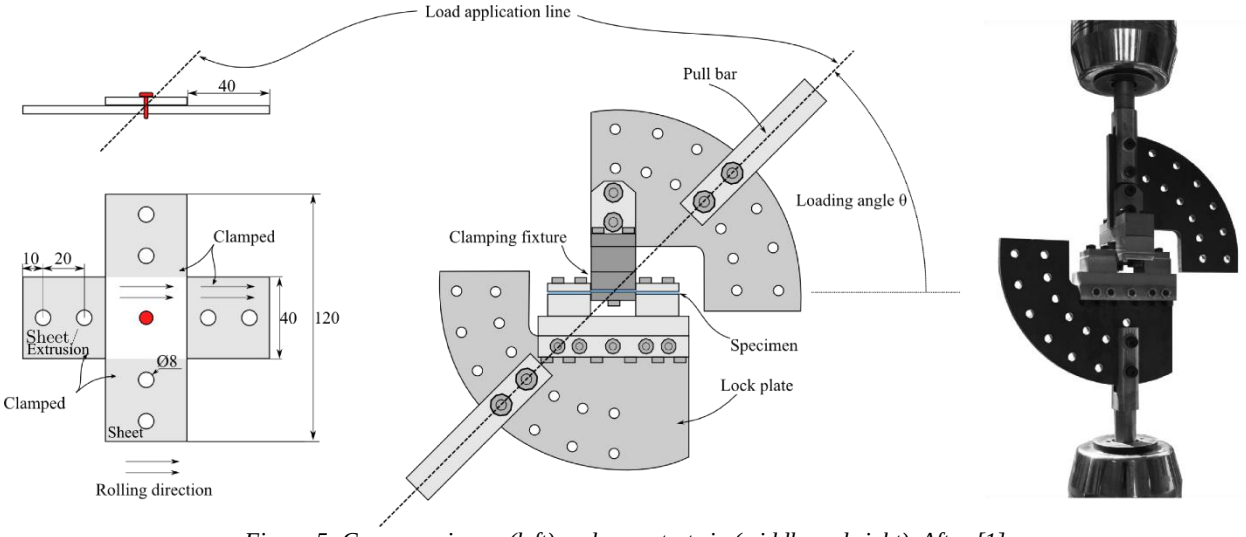

Figure 5: Cross specimens (left) and cross test rig (middle and right). After [1].

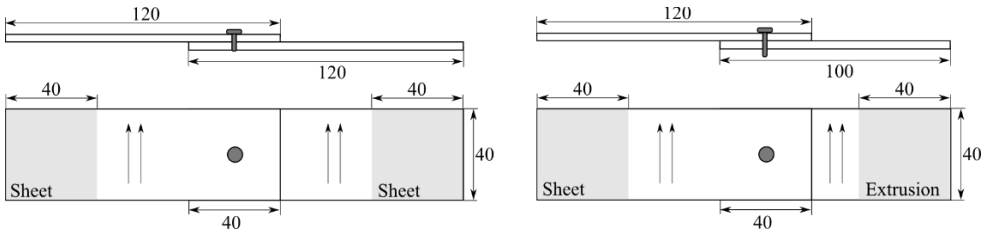

Figure 6: Single lap joint specimens. After [1].

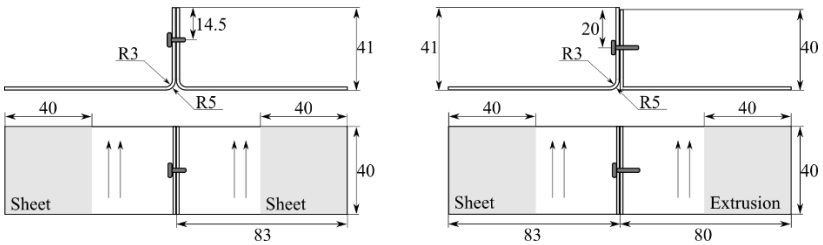

Figure 7: Peeling specimens. After [1].

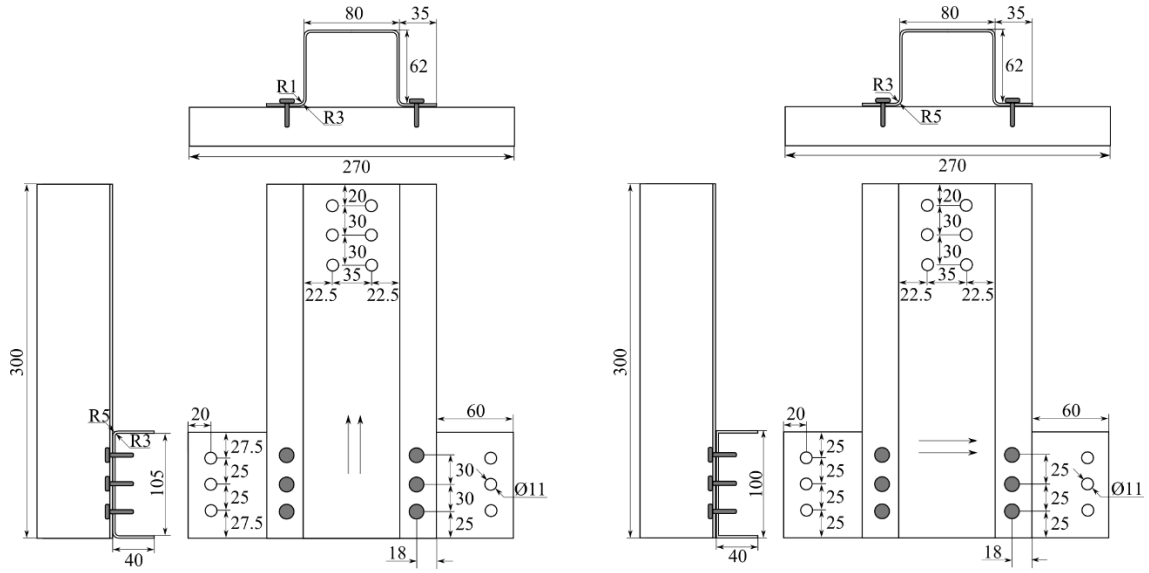

Figure 8: T-component specimens.

In addition to the single connector tests described above, T-component tests were performed for the small and the large FDS connection. Figure 8 shows the T-component specimens used. The U-shaped beam was clamped and fixed in each end, and the top-hat section was clamped and pulled upwards. Cf. [7] for a detailed description of the test set-up. The T-component test represent more complex and uncontrolled macroscopic loadings on the connections. Therefore, it was used for validating the models at a higher level of complexity. The T-component test was not performed for the SPR connection.

FE models

The plates were modelled using Belytschko-Tsay shell elements with full integration with a mesh size of 2x2 mm. To limit the present study, the effect of mesh size in the plates was not investigated. Five integration points were used through the thickness. For contact between the different parts, a surface-to-surface algorithm with a penalty formulation was applied with a static friction coefficient of 0.2. For modelling the materials, an anisotropic yield surface was used with the associated flow rule and an isotropic hardening law. One plane of symmetry was utilised in the T-component simulation. The clamped parts were modelled as rigid bodies, and clamping was represented by constraining displacements. Loads were applied by enforcing displacements in the loading directions while constraining the other directions. Time scaling was applied to limit the computational time of the quasi-static tests. The FE models are shown in Figure 9.

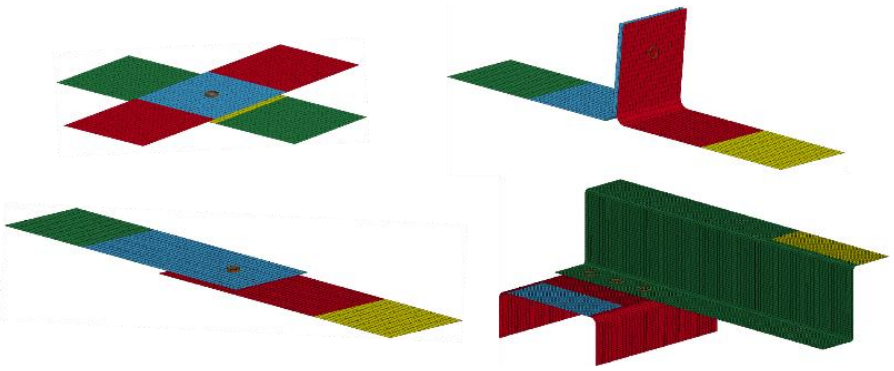

Figure 9: FE models used: cross (top left), single lap joint (bottom left), peeling (top right) and T-component (bottom right).

Calibration

The tensile and shear parameters of both models were identified by reverse engineering the cross tension and cross shear tests, and the mixed-mode parameters of the new model was found by reverse engineering the cross mixed tests. Force-displacement curves from the simulations were compared to the cross-head force and displacement in the experiments. The software LS-OPT® was used to optimize the model parameters.

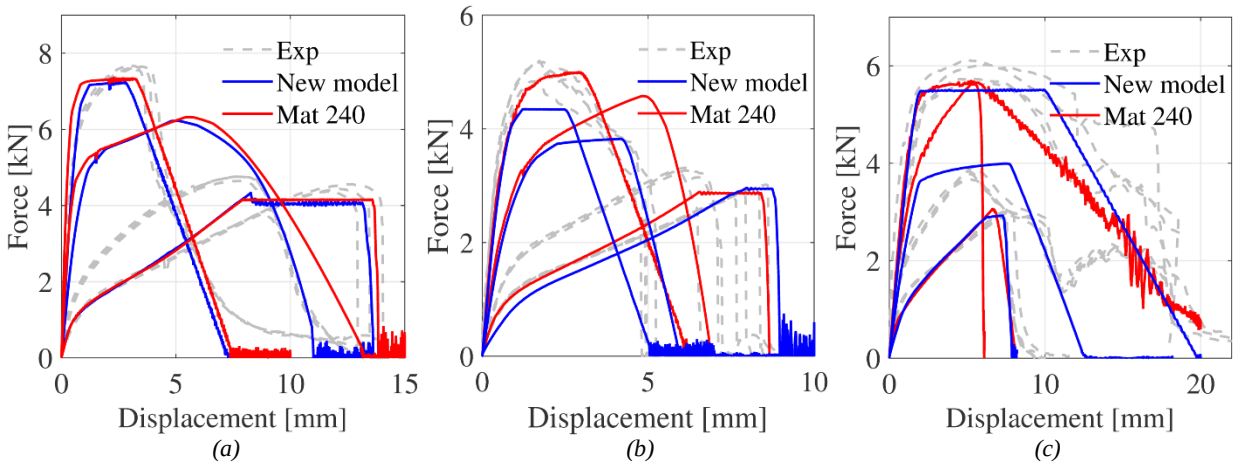

*Figure 10: Results from calibration of the new model compared to *MAT_240 for (a) the SPR connection, (b) the small FDS connection and (c) the large FDS connection.*

Figure 10 shows the results from the calibrations of the new model compared to *MAT_240 for the three connections. As seen in Figure 10 (a), the new model formulation did not significantly affect the ability to describe the SPR connections; both models over-estimated the force in the mixed mode. The new model predicted the ductility more accurate. For the small FDS connection (Figure 10 (b)) it is seen that the new model gave slightly better results in the mixed mode. On the other hand, a significant improvement was observed for the large FDS connection (Figure 10 (c)), as a better description of the mixed mode was obtained both with respect to maximum force and ductility.

When calibrating the mixed-mode parameters it was necessary to keep the exponent parameters α_1, α_2 and α_3 above 1. For a value of 1, Equation (5), (6) and (7) correspond to lines. Below this value, the model behaviour close to pure shear and pure tension became too sensitive to variations in mode mixity (γ). Due to deformations of the shell surfaces in the cross tension and

shear simulations, the mode-mixity angle γ deviated slightly from 0 and $\frac{\pi}{2}$, respectively. That is, the cohesive elements did not undergo "pure" tension and shear. Therefore, although it in some cases gave better response in the cross mixed simulations, exponent values below unity severely impacted the response in the cross tension and shear simulations. This is not desirable, and therefore exponent values below unity is not recommended.

Validation

Figure 11 shows the results from the validation simulations for the SPR connection. The results confirmed the observations from the cross simulations; the new model did not significantly improve the ability to describe the SPR connections. Both models over-estimated the ductility in the single lap-joint test, and the maximum force level in the peeling tests.

Similar results were seen for the small FDS connection (Figure 12). The two models gave similar and satisfying results in the validation simulations.

For the large FDS connection (Figure 13) larger discrepancies between the two models were observed. This was expected, as the mixed-mode behaviour of the two models differed significantly (recall Figure 10 (c)). While *MAT_240 over-estimated the force level and under-estimated the ductility in the single lap-joint tests, the new model under-estimated the force level and over-estimated the ductility. For the peeling test, both models under-estimated the force level and ductility, with the new model performing slightly better. Both models gave a reasonable prediction of the T-component test, with the new model slightly under-predicting the maximum force level.

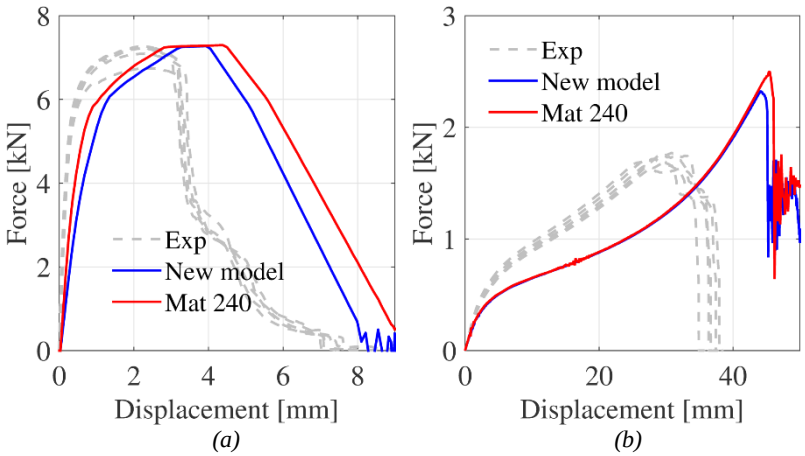

Figure 11: Validation simulations for the SPR connection, (a) single lap-joint and (b) peeling test.

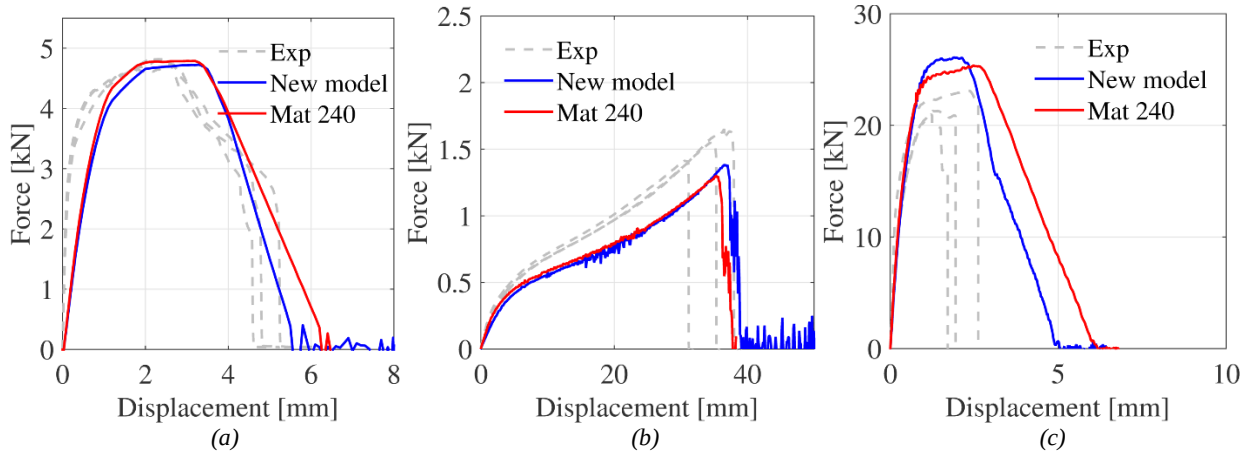

Figure 12: Validation simulations for the small FDS connection, (a) single lap-joint, (b) peeling and (c) T-component test.

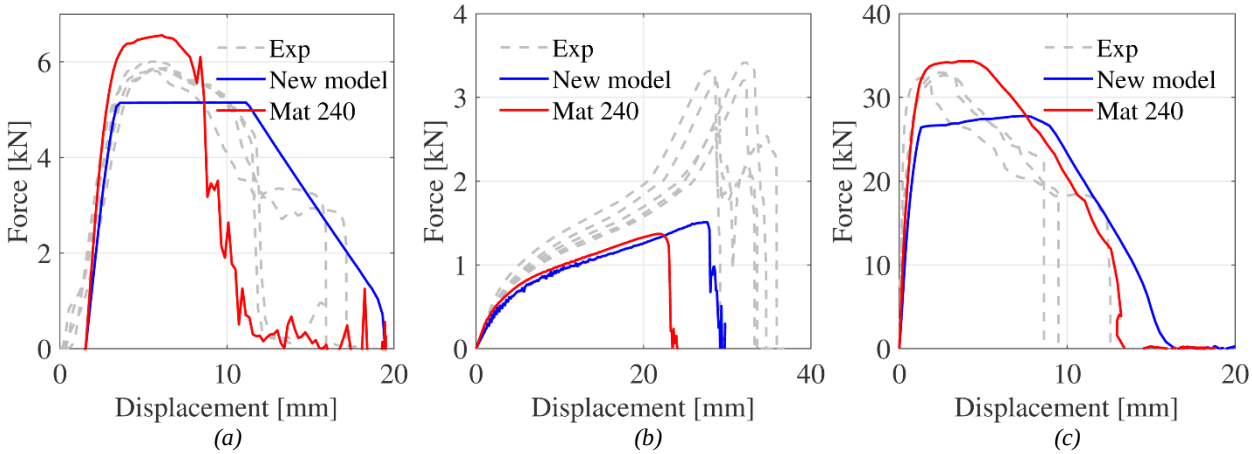

Figure 13: Validation simulations for the large FDS connection, (a) single lap-joint, (b) peeling and (c) T-component test.

Conclusions

- A new cohesive element model based on *MAT_240 for use in large-scale analyses in LS-DYNA has been presented. The new model has added flexibility to control the mixed-mode behaviour.
- The new model was developed in the context of simulating point-connections such as self-piercing rivet and flow-drill screw connections.
- It was demonstrated by three sets of experimental data. One set with mechanical tests on a self-piercing rivet connection, and two sets with two different flow-drill screw connections. Each data set consisted of cross tests in tension, mixed-mode and shear, single lap-joint and peeling tests, and (for the flow-drill screw connections) T-component tests.
- The new model formulation did not significantly affect simulations of the self-piercing rivet connection.
- For the small flow-drill screw connection a slight improvement was observed in the description of the mixed-mode tests.
- For the large flow-drill screw connection a significant improvement was obtained for the mixed-mode simulation.
- Thus, it has been shown that the new cohesive element formulation improves the ability to describe flow-drill screw connections.

References

[1] J. K. Sønstabø, D. Morin, and M. Langseth, "Macroscopic Modeling of Flow-Drill Screw Connections," presented at the 10th European LS-DYNA Conference, 2015.

[2] S. Sommer and J. Maier, "Failure modeling of a self piercing riveted joint using ls-dyna," in *8th European LS-DYNA conference*, 2011.

[3] S. Marzi, O. Hesebeck, M. Brede, and F. Kleiner, "A rate-dependent, elasto-plastic cohesive zone mixed-mode model for crash analysis of adhesively bonded joints," in *7th European LS-DYNA conference*, 2009.

[4] J. O. Hallquist, "LS-DYNA theory manual," *Livermore Software Technology Corporation*, vol. 3, 2006.

[5] M. Bier, C. Liebold, A. Haufe, and H. Klamser, "Evaluation of a Rate-Dependent, Elasto-Plastic Cohesive Zone Mixed-Mode Constitutive Model for Spot Weld Modeling," presented at the 9. LS-DYNA forum, Bramberg, 2010.

[6] J. K. Sønstabø, P. H. Holmstrøm, D. Morin, and M. Langseth, "Macroscopic strength and failure properties of flow-drill screw connections," *Journal of Materials Processing Technology*, vol. 222, pp. 1-12, 2015.

[7] N.-H. Hoang, A.-G. Hanssen, M. Langseth, and R. Porcaro, "Structural behaviour of aluminium self-piercing riveted joints: An experimental and numerical investigation," *International Journal of Solids and Structures*, 2012.